A computational model of open-irrigated radiofrequency catheter ablation accounting for mechanical properties of the cardiac tissue

Argyrios Petras[1,*], Massimiliano Leoni[1,2], Jose M. Guerra[3], Johan Jansson[1,2], and Luca Gerardo-Giorda[1]

[1]BCAM - Basque Center for Applied Mathematics, Bilbao, Spain
[2]Department of Computational Science and Technology, KTH Royal Institute of Technology, Stockholm, Sweden
[3]Department of Cardiology, Hospital de la Santa Creu i Sant Pau, Barcelona, Spain
[*]Alameda de Mazarredo 14, 48009 Bilbao, Bizkaia, Spain, apetras@bcamath.org

October 4th, 2018

Abstract

Radiofrequency catheter ablation (RFCA) is an effective treatment for cardiac arrhythmias. Although generally safe, it is not completely exempt from the risk of complications. The great flexibility of computational models can be a major asset in optimizing interventional strategies, if they can produce sufficiently precise estimations of the generated lesion for a given ablation protocol. This requires an accurate description of the catheter tip and the cardiac tissue. In particular, the deformation of the tissue under the catheter pressure during the ablation is an important aspect that is overlooked in the existing literature, that resorts to a sharp insertion of the catheter into an undeformed geometry. As the lesion size depends on the power dissipated in the tissue, and the latter depends on the percentage of the electrode surface in contact with the tissue itself, the sharp insertion geometry has the tendency to overestimate the lesion obtained, especially when a larger force is applied to the catheter. In this paper we introduce a full 3D computational model that takes into account the tissue elasticity, and is able to capture the tissue deformation and realistic power dissipation in the tissue. Numerical results in FEniCS-HPC are provided to validate the model against experimental data, and to compare the lesions obtained with the new model and with the classical ones featuring a sharp electrode insertion in the tissue.

Keywords: radiofrequency ablation; open-irrigated catheter; elastic tissue deformation; finite elements

1 Introduction

Radiofrequency catheter ablation (RFCA) is a minimally invasive therapy widely used for the treatment of various types of cardiac arrhythmias [1, 2]. Typically, for endocardial radiofrequency

ablations (RFA), a catheter is advanced into the cardiac chamber from the groin of the patient through a blood vessel. Radiofrequency (RF) current at $500\,\mathrm{kHz}$ is delivered to the arrhythmogenic tissue via the electrodes on the catheter, producing resistive electrical heating in the neighborhood of the electrode. Conduction then propagates the heating through the rest of the tissue. At a target temperature, usually of $50\,^{\circ}\mathrm{C}$, irreversible damage is inflicted to the tissue and a lesion is formed [1].

RFA is considered an effective and safe treatment for cardiac arrhythmias, however a number of life threatening complications may occur. Excessive heating of the blood near the electrode reaching around $80\,^{\circ}\mathrm{C}$ leads to the denaturation of the blood proteins and the formation of a coagulum at the tip of the catheter [1, 3]. In addition, extreme heating of the tissue at $100\,^{\circ}\mathrm{C}$ leads to steam formation and audible steam pops occur [4, 5, 6], which could result in myocardial tear or tamponade [1].

Several computational models have been developed to describe the biophysics of the cardiac RFA treatment process. Some use an axisymmetric approach and develop 2-D geometries, on which they employ Penne's bioheat equation with convective boundary conditions for the cooling effect of the blood flow, coupled with a quasi-static electrical potential equation [7, 8, 9, 10]. To model the effect of the coolant liquid of open irrigated catheters, these models typically fix the temperature of the tip electrode [11, 12].

Three dimensional cardiac RFA models that use the same mathematical equations as the 2-D axisymmetric models are also available [13, 14, 15]. For open irrigated catheters, some models include the interaction of the saline inflow with a layer of saline in epicardial modelling [16] or with the surrounding blood in endocardial RFA [17]. Typically, a sharp insertion of the catheter in the tissue is considered, disregarding its elastic deformation. However the need for the incorporation of mechanical deformation in RFA modelling was hinted in a previous work [15]. Indeed, the amount of power delivered to the tissue depends on the surface of contact between the electrode and the tissue itself [18]. Sharp insertion produces larger surfaces of contact, and is likely to overestimate the actual effect of the RFA treatment. The first RFA model that includes elastic deformation of the tissue uses profiles that are extracted from X-ray scanning before the ablation process [19]. No other work was found in our literature review that includes the tissue deformation due to the contact with the catheter.

We propose a computational model that includes both physical and mechanical properties of the tissue. We consider in this work a 6-holes open electrode with a hemispherical tip, placed vertically on the cardiac tissue. We model the elastic deformation of the tissue in contact with the tip by solving the axisymmetric Boussinesq problem for a spherical punch. We use a modified version of Penne's bioheat equation to model the thermal effect of RFA and a quasi-static electrical potential equation. Constant-power ablation is obtained by augmenting the system with a power constraint equation. The model also features the incompressible Navier-Stokes equations to describe the flow of blood and the saline flow from the open-irrigated electrode. We validate our proposed computational model against a set of suitably defined *in-vitro* experiments performed at J.M. Guerra's lab at the Hospital de la Santa Creu i San Pau in Barcelona. We investigate the effect of tissue elasticity in the computational RFA models by comparing the computational lesion dimensions of the deformed tissue case against the undeformed one that is typically used in state-of-the-art models.

The paper unfolds as follows. Section 2 describes our mathematical model, and in Section 3 we describe its calibration. In Section 4 we validate the proposed model against a set of *in-vitro* experiments: we describe the experimental setup and discuss the results of the proposed

2

computational model. We also compare the results of our model with the ones obtained with a geometry featuring a sharp insertion of the electrode. Finally, in Section 5 we discuss our findings and the limitations of the proposed model and suggest some ways to overcome them.

2 Computational model

Our mathematical model consists of a system of partial differential equations that describe the evolution of the temperature, the flow of blood and the cooling saline solution, as well as the electrical field generated by the RFA procedure. In this section, we expand on its main characteristics: the geometry, the governing equations, and the method to assess the computational lesion.

2.1 Geometry

The computational domain that we consider in this paper is based on an *in-vitro* experimental setup, which is similar to the one presented by Guerra et al. [20]. We construct a box of dimensions $80\,\text{mm} \times 80\,\text{mm} \times 80\,\text{mm}$ that consists of the blood chamber $80\,\text{mm} \times 80\,\text{mm} \times 40\,\text{mm}$, the cardiac tissue $80\,\text{mm} \times 80\,\text{mm} \times 20\,\text{mm}$, and a board $80\,\text{mm} \times 80\,\text{mm} \times 20\,\text{mm}$ underneath the tissue. The board separates the tissue from the dispersive electrode, that is located at the bottom of the computational domain. This is an important aspect, matching the settings in the experiments used for validation, where the tissue is not in direct contact with the dispersive electrode, but is actually placed on a physical board of methacrylate. Moreover, in clinical RFA, the dispersive electrode is placed on a patch on the back (or thigh) of the patient. Having the dispersive electrode in direct contact with the tissue would lead to an excessive simplification of the model. Also, the presence of the board allows us to match the impedance of the RFA system (provided by the machine) without modifying the electrical conductivity of the tissue.

We place a catheter perpendicular to the tissue at the center of the box inside the blood chamber, causing a deformation that depends on the catheter-tissue contact force (see Section 2.5). Figure 1 (left) shows the described computational geometry. We consider a 6-holes open-irrigated electrode of diameter 2.33 mm and length 3.5 mm with a hemispherical tip. The electrode contains a thermistor of diameter 1.54 mm and length 3 mm. The holes, of diameter 0.5 mm, are connected to an inner channel of diameter 0.73 mm inside the thermistor, which is connected to the catheter body and allows the saline to flow in the blood chamber. Figure 1 (right) shows the geometry of the open-irrigated electrode.

The computational domain consists of five different subdomains: the blood chamber (Ω_{blood}), the cardiac tissue (Ω_{tissue}), the external factors board (Ω_{board}), the electrode (Ω_{el}) and the thermistor (Ω_{therm}). In what follows, we will simply denote

$$\Omega := \Omega_{blood} \cup \Omega_{tissue} \cup \Omega_{board} \cup \Omega_{el} \cup \Omega_{therm}.$$

The catheter body and the inner tubes at the open-irrigated electrode are considered thermally and electrically insulated, and therefore insulation boundary conditions are applied. Additional details on the thermal and electrical boundary conditions are provided in Sections 2.3 and 2.4.

2.2 Blood and saline flow

The open-irrigated electrode allows the cooling saline to flow out through the holes at its tip, and mix with the blood. The comparable densities between saline and blood justifies the assumption
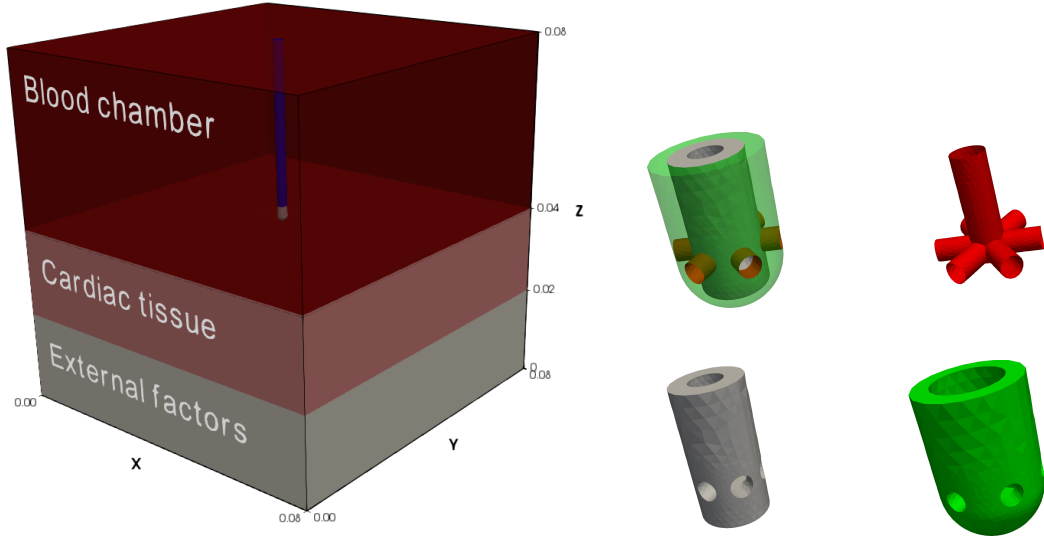
Figure 1: Left: The full computational geometry. Right: Detailed view of the catheter tip and its components. Top left to bottom right: the assembled catheter tip, the saline pipes, the thermistor, and the electrode.

of a perfect mix in the blood chamber. The flow dynamics is thus governed by the incompressible Navier-Stokes equations:

$$
\begin{aligned}
\frac{\partial \boldsymbol{u}}{\partial t} + \boldsymbol{u} \cdot \nabla \boldsymbol{u} - \operatorname{div} \sigma(\boldsymbol{u}, p) &= \boldsymbol{0} \\
\operatorname{div} \boldsymbol{u} &= 0
\end{aligned}
\tag{1}
$$

where $\boldsymbol{u}$ is the flow velocity, p is the pressure scaled by the density ρ and $\sigma(\boldsymbol{u}, p) = 2\mu\rho^{-1}\frac{\nabla\boldsymbol{u}+\nabla\boldsymbol{u}^T}{2} - pI$ is the stress tensor, μ being the dynamic viscosity of the blood.

We impose zero pressure and stress as an outflow boundary condition on the right side of the domain $\{x = 0.08\}$. A constant inflow boundary condition is imposed on the left side of the domain $\{x = 0\}$,

$$
\boldsymbol{u} = \boldsymbol{u}_{in} = (u_b, 0, 0),
$$

and on the electrode holes for the flow of the coolant liquid,

$$
\boldsymbol{u} = u_s \boldsymbol{n}_e,
$$

where u_b and u_s are the magnitudes of the velocity of the blood and the coolant liquid respectively, while $\boldsymbol{n}_e$ is the unit normal vector of the electrode pointing towards the blood chamber. All the remaining boundaries, including the internal one separating the blood chamber from the tissue, are equipped with no-slip boundary conditions. See Figure 3 for a representation of all boundary conditions.

4

2.3 Electrical field

The electrical field is generated by the electrode at the tip of the catheter. At a frequency of $500\,\mathrm{kHz}$, and over the distance of interest, the biological medium can be considered totally resistive and the electrical problem can be set in quasi-static form:

$$\operatorname{div}(\sigma(T)\nabla\Phi) = 0, \tag{2}$$

where Φ is the electrical potential. We consider the electrical conductivity $\sigma = \sigma(T)$ (not to be confused with the stress tensor $\sigma(\boldsymbol{u}, p)$ introduced in (1)) to be constant in all regions but in the tissue, where we consider a linear dependency on the temperature (see Section 3.1).

For a constant-power ablation mode, equation (2) is augmented with a constant-power constraint [21]

$$\int_\Omega \sigma(T)\nabla\Phi \cdot \nabla\Phi \ \mathrm{d}x = P, \tag{3}$$

where Ω is the computational domain and P is the constant power imposed.

We set an initial potential of $0\,\mathrm{V}$ everywhere. We impose a zero potential condition on the bottom of the domain to model the dispersive electrode, while on the remaining external surfaces and the catheter boundary we assign an insulation condition ($-\sigma\nabla\Phi \cdot n = 0$).

2.4 Tissue heating

The application of an electrical potential at the tip electrode of the catheter produces resistive heating at the cardiac tissue and the surrounding blood. A modification of Penne's bioheat equation models both the heating by the direct application of RF current and the conductive heating [17] and reads

$$\frac{\partial(\rho h)}{\partial t} - \operatorname{div}(k(T)\nabla T) = q - \rho c(T)\boldsymbol{u} \cdot \nabla T + Q_m - Q_p, \tag{4}$$

where ρ is the density, h is the specific enthalpy, $c(T)$ is the specific heat, $k(T)$ is the thermal conductivity of the medium, $q = \sigma(T)|\nabla\Phi|^2$ is the distributed heat source from the electrical field, Q_m is the metabolic heat generation and Q_p is the heat loss due to the blood perfusion. For endocardiac RFA, the last two terms in this equation can be omitted for short ablation times [14, 17, 22].

In biological tissues, the specific enthalpy h and the temperature T are related as follows:

$$\frac{\partial(\rho h)}{\partial t} = \psi(T)\frac{\partial T}{\partial t},$$

where $\psi(T) = \rho c(T)$. Finally, we assume the thermal conductivity $k(T)$ and the specific heat $c(T)$ to be piecewise constant, with different values in different regions of the domain, except in the tissue, where we consider a linear dependence on the temperature (see Section 3.1).

The final form of the bioheat equation is then

$$\rho c(T)\left(\frac{\partial T}{\partial t} + \boldsymbol{u} \cdot \nabla T\right) - \operatorname{div}(k(T)\nabla T) = \sigma(T)|\nabla\Phi|^2. \tag{5}$$

2.5 Elasticity

During the ablation procedure, the electrode at the tip of the catheter applies a contact force to the cardiac tissue, resulting in its deformation. For a catheter with a hemispherical tip such as the one we consider in this paper (see Figure 1), the problem is equivalent to a spherical indenter on an elastic half-space in contact mechanics. There are many different approaches for this contact mechanics problem, including Hertzian theory for shallow indentations [23, 24], a modified Hertzian solution [25] and the axisymmetric Boussinesq problem [26]. We use the axisymmetric Boussinesq problem approach as it provides a general framework for different profiles, which will allow us to consider also different catheter tips in the future. In this work we consider a spherical indenter profile.

Following [26], due to the radial symmetry of the contact problem, consider the two dimensional problem on the vertical z-axis and the horizontal r-axis, which represents the distance from the center of the sphere. The deformed elastic tissue follows the spherical indenter from the center of the sphere, where the maximum vertical displacement ω_{max} occurs, up to the contact radius a. After the contact point, the elastic tissue deformation is smoothly decreasing as the distance r increases. Figure 2 shows the deformation of the tissue, as described.
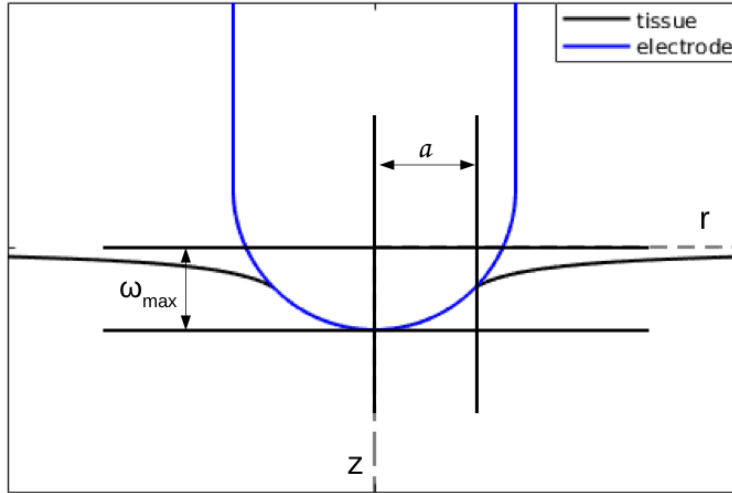

Figure 2: A cross-section of the electrode-tissue contact.

Thus, for the case $r \leq a$, the elastic tissue follows the sphere, i.e.

$$r^2 + [z + (R - \omega_{\mathrm{max}})]^2 = R^2,$$

where R is the radius of the sphere. The positive solution of this system for z gives the displacement of the interface $\omega(r)$ as a function of the distance r,

$$\omega(r) = \omega_{\mathrm{max}} - f(r/a), \tag{6}$$

where $f(t) = R - \sqrt{R^2 - a^2 t^2}$. The function f is the profile of the spherical indenter that is used in the rest of the computations.

The maximum depth is given by the formula

$$\omega_{\max} = \frac{a}{2} \log \left(\frac{R + a}{R - a} \right),$$ (7)

and the total force is

$$F = \frac{G}{1 - \nu} \left((a^2 + R^2) \log \left(\frac{R + a}{R - a} \right) - 2aR \right),$$ (8)

where ν is the Poisson's ratio and

$$G = \frac{E}{2(1 + \nu)}$$

is the shear modulus of the tissue, E being the Young's modulus of elasticity.

For $r > a$, the deformation can be calculated by evaluating the integral

$$\omega(r) = \int_0^1 \frac{\chi(t)}{(r/a)^2 - t^2} \, dt,$$ (9)

where

$$\chi(t) = \frac{2\omega_{\max}}{\pi} - \frac{at}{\pi} \log \left(\frac{R + at}{R - at} \right).$$

Thus, given the contact force F, the contact radius a can be calculated by Equation (8) using optimization techniques. The remaining quantities can be calculated using the corresponding formulas above. The displacement of the interface $\omega(r)$ is calculated using numerical integration techniques for $r > a$.

2.6 Model summary

We consider a 3D computational geometry, as described in Section 2.1, and we compute the vertical displacement of the surface of the tissue for a given catheter contact force (see Section 2.5).

We summarize the mathematical model in the following system of coupled PDEs:

$$\frac{\partial \boldsymbol{u}}{\partial t} + \boldsymbol{u} \cdot \nabla \boldsymbol{u} - \operatorname{div} \sigma(\boldsymbol{u}, p) = \boldsymbol{0} \qquad \text{in } \Omega_{blood} \times (0, T),$$ (10a)

$$\operatorname{div} \boldsymbol{u} = 0 \qquad \text{in } \Omega_{blood} \times (0, T),$$ (10b)

$$\rho c(T) \left(\frac{\partial T}{\partial t} + \boldsymbol{u} \cdot \nabla T \right) - \operatorname{div} (k(T)\nabla T) = \sigma(T)|\nabla \Phi|^2 \qquad \text{in } \Omega \times (0, T),$$ (10c)

$$\operatorname{div} (\sigma(T)\nabla \Phi) = 0 \qquad \text{in } \Omega \times (0, T).$$ (10d)

The above equations are equipped with a number of different boundary conditions, applied to the various parts of our computational geometry. Figure 3 collects the boundary conditions of (10a)-(10d): unless stated otherwise, we impose zero velocity ($\boldsymbol{u} = \boldsymbol{0}$), zero current flux ($\sigma\nabla\Phi \cdot n = 0$) and body temperature ($T = T_b = 37\,°\text{C}$) on all the surfaces of the boundary. We impose zero velocity on the tissue surface, which is part of the boundary of Ω_{blood}. The values of the saline inlet $\boldsymbol{u}_s$ are given by the RF protocol under consideration. The homogeneous Dirichlet boundary condition for the potential $\Phi = 0$ on the bottom surface models the dispersive electrode, while the Dirichlet condition $\Phi = V_0$ on the upper boundary of the electrode is discussed in the upcoming Sections 3.1.2 and 3.1.3. We set the initial conditions to $p = 0$, $\boldsymbol{u} = \boldsymbol{0}$, $\Phi = 0$ and $T = T_b$ in the whole domain.
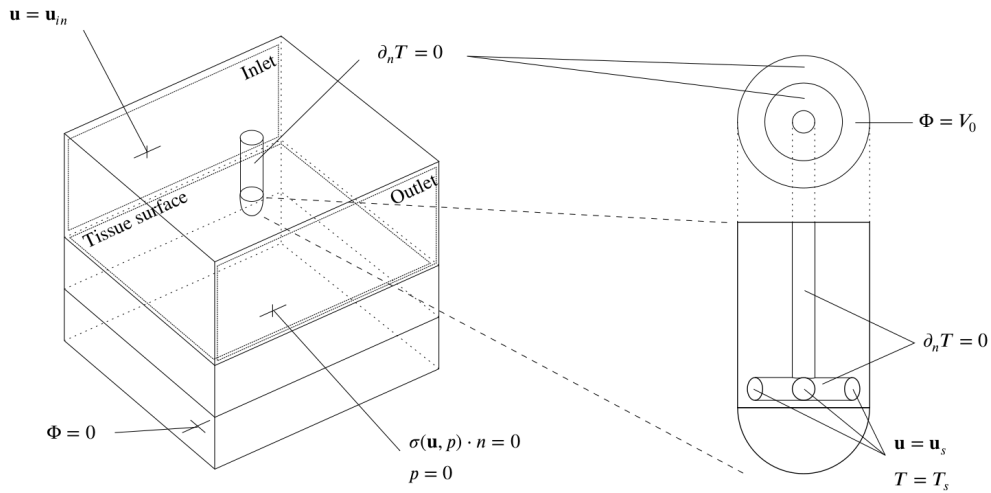
Figure 3: Boundary conditions that differ from zero velocity ($\boldsymbol{u} = \boldsymbol{0}$), zero current flux ($\sigma \nabla \Phi \cdot n = 0$) and body temperature ($T = T_b$).

2.7 Lesion assessment

The prediction of the lesion size is important to ensure the effectiveness of RF treatment. During the ablation process, RF current flows through the myocardium and, via Joule heating, a rise in the tissue temperature is produced in a small area around the electrode tip. The tissue is irreversibly damaged and a thermal lesion is formed when the temperature rises above 50 °C [1]. In light of the above consideration, we assume that a lesion is fully formed at the isotherm contour of 50 °C. In order to assess the lesion characteristics, typical quantities of interest are its depth (D), width (W), depth at which the maximal width occurs (DW), as well as its volume (V). Also, the area of the lesion on the tissue surface (S) is important to study the possible formation of thrombi. The characteristic dimensions we consider in this paper to validate the computational model are described in Section 4.2, and collected in Figure 4 therein.

3 Calibration of the model

3.1 Model parameters

The parameters considered in this paper are drawn from the literature and are summarized in Table 1. Specifically, the physical properties of the blood are obtained from the virtual population database from the IT IS foundation [27]. The electrode and thermistor physical properties were found in the literature [15, 17]. We assume the electrical conductivity of the external factors board σ_b to be constant and we tune it to match the initial impedance of the experimental setup, as detailed in Section 3.1.2. We choose the remaining parameters for the board to be the same as the initial tissue state; they appear to have no impact on the results of our numerical simulations.

Considering that in our *in-vitro* experiments RFA was performed on a porcine myocardium, we

Parameter	Blood	Tissue	Electrode	Thermistor	Board
ρ (kg m^{-3})	1050	1076	21500	32	1076
c (J kg^{-1} K^{-1})	3617	$c_0 = 3017$	132	835	3017
k (W m^{-1} K^{-1})	0.52	$k_0 = 0.518$	71	0.038	0.518
σ (S m^{-1})	0.748	$\sigma_0 = 0.54$	4.6×10^6	10^{-5}	σ_b
$\mu\rho^{-1}$ (m^2 s^{-1})	2.52×10^{-6}	-	-	-	-
ν (-)	-	0.499	-	-	-
E (kg m^{-1} s^{-2})	-	75×10^3	-	-	-

Table 1: The parameters we considered in our proposed computational model.

used the corresponding physical properties [28, 29, 30]. We use a linear temperature-dependence of specific heat, thermal and electrical conductivities of the tissue according to the aforementioned literature:

$$c(T) = c_0(1 - 0.0042(T - 37)), \qquad k(T) = k_0(1 - 0.0005(T - 37)), \qquad \sigma(T) = \sigma_0(1 + 0.015(T - 37))$$

where c_0, k_0 and σ_0 are the specific heat, the thermal and the electrical conductivities at body temperature (see Table 1). Finally, since the experiments were performed in an *in-vitro* condition, it is reasonable to assume that the cardiac tissue got stiffer during preparation. We thus used in our simulations the Young's modulus of the cardiac tissue at systole [47], which is within the range of measurements in an *in-vitro* experimental setup found in [48].

3.1.1 Tissue power delivery calibration

In our model, we set the electrical conductivity of the board σ_b to match the power dissipated in the tissue P_{tissue}, that we identify following the analysis of Wittkampf and Nakagawa in [18]: the percentage of the total power P delivered to the tissue is given by the formula:

$$P_{tissue} = \frac{A_{tissue}\sigma_{tissue}}{A_{blood}\sigma_{blood} + A_{tissue}\sigma_{tissue}} P =: \alpha P, \tag{11}$$

where P is the total power set by the machine in the experiment and A_{blood} and A_{tissue} is the contact area of the electrode with the blood and the tissue respectively.

In our computational geometry (see Section 2.1) we chose a hemispherical catheter tip. Thus, the surface area of the catheter in contact with the tissue A_{tissue} can be calculated as follows

$$A_{tissue} = \begin{cases} 2\pi R h, & \text{if } h \leq R, \\ 2\pi R^2 + 2\pi R(h - R) - 6R_h^2 \cos^{-1}\left(1 + \frac{R-h}{R_h}\right), & \text{if } R < h \leq R + R_h \\ 2\pi R^2 + 2\pi R(h - R) - 6R_h^2 \left(\frac{\pi}{2} + \cos^{-1}\left(2 + \frac{R-h}{R_h}\right)\right), & \text{if } R + R_h < h \leq R + 2R_h \\ 2\pi R^2 + 2\pi R(h - R) - 6\pi R_h^2, & \text{if } h \geq R + 2R_h, \end{cases}$$

where $h = \omega_{\max} - \omega(a)$ is the contact depth of the catheter with the tissue (see Section 2.5) and R_h is the radius of the irrigation holes on the catheter (see Section 2.1). The blood surface area is calculated using the formula

$$A_{blood} = 2\pi R^2 + 2\pi R(h_e - R) - 6\pi R_h^2 - A_{tissue},$$

where h_e is the length of the electrode.

3.1.2 External factors calibration

We included the external factors board in the model to represent the part of the experimental setup, between the tissue and the dispersive electrode, that is not modelled. We tune the external-factors board's conductivity σ_b to match the actual power delivered to the tissue as described in Section 2. This approach allows us to use as much of the information available from the RFA system as possible, and provides us with great flexibility should different types of tissue be considered, in a major improvement with respect to standard approaches on the topic (including earlier works by some of the authors [17]) that tuned the tissue conductivity to match the overall system's initial impedance.

Given the total power of the ablation P and the initial impedance of the system R, (both values available from the RFA system), the initial potential drop in the system is given by Ohm's law as $V_0 = \sqrt{PR}$. We can assume that the electrode cable is not dissipating energy, thus we can consider the potential drop to occur entirely between the cable-electrode junction and the dispersive electrode. We thus impose a Dirichlet boundary condition on the upper boundary of the electrode (see Figure 3), and we solve the potential equation in the whole domain Ω. The advantage of such a framework is that the interfaces between different materials are actually internal discontinuity surfaces of the domain: the equation itself takes care of the conductances drop across internal layers as a consequence of the solution's continuities [33]. In addition, modifications of the electrode material would be immediate.

The calibration of the external factors board conductivity is an iterative pre-processing step. Given an initial guess of σ_b, we solve equation (10d) with $V_0 = \sqrt{PR}$ as boundary condition, and suitably update the value of σ_b, until the constraint

$$\int_{\Omega_{tissue}} \sigma_0 |\nabla \Phi|^2 \, \mathrm{d}x = P_{tissue} \tag{12}$$

is satisfied, P_{tissue} being the one in (11). In the code developed to obtain the results of Section 4, we implement a root-finding algorithm via bisection search, that stops once the difference between two subsequent iterations is smaller than $0.01\,\mathrm{W}$. The calculated σ_b is kept constant throughout the simulation.

3.1.3 Voltage calibration during the simulation

In Section 2.3 no boundary conditions were specified for the potential equation at the upper part of the electrode, but we required the solution to satisfy a constraint on the total dissipated power (3). However, due to the difference in size between our computational domain and the actual ablation site, the total power dissipated in the computational setting is expected to be smaller than the one provided by the machine. We assume the power dissipated outside our computational domain as well as the one in Ω to be constant in time. During the simulation we update the potential V_0 on the upper interface of the electrode, so that the solution satisfies

$$\int_{\Omega} \sigma |\nabla \Phi|^2 \, \mathrm{d}x = P_0. \tag{13}$$

In the above formula, P_0 is the total power dissipated in our computational domain at the beginning of the simulation with σ_b computed as described in the previous section. We assume a constant voltage on the surface where we impose the boundary condition: the electrode is made of conductive material and we know from standard theory of electromagnetism that electrons can move freely on the surface of a conductor, tending to a configuration of equilibrium.

4   Numerical Results

For the simulations in this work, we built a 3D computational geometry for each given catheter contact force, where the vertical displacement of the surface of the tissue is computed by means of a Clenshaw-Curtis numerical integration method [34].

The resulting domain Ω is discretized by a tetrahedral unstructured mesh, with adaptive refinement in the neighborhood of the electrode. The mesh is built with Salome [35]. For all the simulations presented in this work, the meshes feature approximately $5\,000\,000$ elements with minimum and maximum element sizes of the order of magnitude of $5 \times 10^{-5}\,$m and $1 \times 10^{-3}\,$m. Following the instructions of the catheter producer, the saline inflow is set at $u_s = 0.24\,$m/s, corresponding to an irrigation rate of $17\,$mL$/$min subdivided among the 6 irrigation holes. In the model validation section, the blood inflow velocity is set to $u_b = 0.5\,$m/s to match our experimental setup described in the upcoming Section 4.2. In the comparison between elastic deformation and sharp insertion, two blood flow protocols are considered, as in the experiments by J. Guerra and his collaborators [20]: a High-Flow protocol (HF) with $u_b = 0.5\,$m/s, and a Low-Flow protocol (LF), with $u_b = 0.1\,$m/s.

4.1   Simulations protocol

Computational modelling of ablation as well as other medical procedures and diagnostics in cardiovascular science represent significant scientific challenges, such as robust turbulent fluid-structure interaction (FSI) with contact and heating, control of the computational error in multiphysics problems, and complex software implementation. For computational technology to be effective in overcoming these challenges, it has to be **efficient**: enabling solution of advanced problems with available resources, **reliable**: providing quantitative error control or the computational solution in a chosen output, as well as a guarantee of correctness of software implementation, and **accessible**: enabling scientists to access, use and extend the simulation technology as a tool in their daily work.

We address these problems in the setting of a general stabilized adaptive finite element methodology we denote Direct FEM Simulation (DFS) [36] realized in the automated massively parallel FEniCS-HPC open source software framework [37, 38], taking the weak form of the partial differential equation (PDE) as input and automatically generating low-level source code for assembling tensors and duality-based a posteriori error estimates and indicators for adaptive error control with good scaling on supercomputers. In this framework, we developed an RFA module in FEniCS-HPC explicitly for the present work to discretize and solve system (10a)-(10d).

Navier-Stokes equations   The Navier-Stokes equations are solved via the DFS method presented in [36, 39, 40], consisting of a standard P1-P1 finite elements method with Galerkin Least-Squares stabilization and optional goal-oriented adaptive mesh refinement. The Navier-Stokes

system is discretized in time by a Crank-Nicholson scheme, and DFS solves the full nonlinear problem via successive minimizations based on a fixed-point approach [36, 40].

Bioheat equation The Bioheat equation, on the other hand, is solved with P1 elements and is advanced in time by a backward Euler scheme, where the coefficients are linearized around the previous time step. Since for the set of parameters introduced in Section 3.1 the Bioheat equation is advection-dominated in Ω_{blood}, an SUPG (Streamline-Upwind Petrov-Galerkin) stabilization term is added to the discrete equation[41].

Potential equation The potential equation is solved with P1 elements. The equation depends implicitly on time through the conductivity. As the simulation proceeds, the rise in the tissue temperature modifies its electrical conductivity, and the constraint on the total dissipated power will eventually fail to be satisfied. We thus enforce constraint (13) at each time step when we solve the potential equation as follows.

Let Φ_1 be the solution of

$$
\begin{aligned}
\operatorname{div}\left(\sigma^{new}\nabla\Phi_1\right) = 0 && \text{in } \Omega \\
\Phi_1 = V_0^{old} && \text{on } \partial\Omega_{el}^{up} \\
\Phi_1 = 0 && \text{on } \partial\Omega^{bottom} \\
\sigma^{new}\nabla\Phi_1 \cdot n = 0 && \text{on } \partial\Omega\backslash\{\partial\Omega_{el}^{up}\cup\partial\Omega^{bottom}\}
\end{aligned}
\tag{14}
$$

where V_0^{old} and σ^{new} are the previous value of the potential on the upper part of the electrode and the new value of the electrical conductivity, respectively. The power dissipated by Φ_1 is

$$
P_1 = \int_\Omega \sigma^{new}|\nabla\Phi_1|^2 \ \mathrm{d}x.
$$

If $|P_1 - P_0| < 0.01\,\mathrm{W}$, we choose $\Phi^{new} = \Phi_1$ as new solution.

On the other hand, if P_1 does not fall within the tolerance, we proceed as follows. By linearity, the function $\Phi_2 = \lambda\Phi_1$ is the solution of problem (14) with Dirichlet boundary condition $\Phi_2 = \lambda V_0^{old}$ on $\partial\Omega_{el}^{up}$ (Dirichlet boundary conditions scale linearly and the Neumann one is itself homogeneous). The power dissipated in the domain by Φ_2 is

$$
P_2 = \int_\Omega \sigma^{new}|\nabla\Phi_2|^2 \ \mathrm{d}x = \int_\Omega \sigma^{new}|\nabla(\lambda\Phi_1)|^2 \ \mathrm{d}x = \lambda^2 \int_\Omega \sigma^{new}|\nabla\Phi_1|^2 \ \mathrm{d}x = \lambda^2 P_1.
$$

By requesting Φ_2 to satisfy constraint (13) (namely, imposing $P_2 = P_0$), we can solve for $\lambda = \sqrt{P_0/P_1}$, and the new potential will be

$$
\Phi^{new} = \sqrt{\frac{P_0}{P_1}}\ \Phi_1, \qquad V_0^{new} = \sqrt{\frac{P_0}{P_1}}\ V_0^{old}.
$$

Time stepping A time step of $\Delta t = 0.01\,\mathrm{s}$ has been used for the bioheat equation and a smaller, adaptively computed time step is used for the Navier-Stokes equations. As a consequence of the different time steps employed, the two models are synchronized at the larger time step, where also the potential equation is solved. Let $t^n = n\Delta t$ be the n-th time step of the bioheat equation, and let $(\boldsymbol{u}_h^n, p_h^n, \Phi_h^n, T_h^n)$ be the numerical solution at time t^n. We can briefly summarize the procedure to advance from t^n to t^{n+1} as follows.

1. Solve the Navier-Stokes equations in (t^n, t^{n+1}) with the adaptive time step and compute, in particular, $\boldsymbol{u}_h^{n+1}$.

2. Solve the potential equation for Φ_h^{n+1} with coefficient $\sigma(T_h^n)$

3. Solve the bioheat equation for T_h^{n+1} using $\boldsymbol{u}_h^{n+1}$ in the transport term, Φ_h^{n+1} in the source term, $\sigma(T_h^n)$, $c(T_h^n)$ and $k(T_h^n)$ as coefficients.

We refer the reader to the supplementary material section for a more detailed description of the numerical discretization. Finally, the lesion dimensions are calculated in a post-processing step in Paraview [42] with self-developed Python-coded filters.

Remark. *Since the stress tensor $\sigma(\boldsymbol{u}, p)$ is independent of the temperature, equations* (10a) *and* (10b) *are in a one-way coupling with the rest of the system. Thus, already in our current situation, but even should the geometry change in time due to a variable pressure during the ablation (as it is the case in clinical RFA procedures), it would still be possible to solve the Navier-Stokes equation independently as a first step and then use the solution to solve equations* (10d) *and* (10c), *potentially for a variety of different protocols. However, we chose to solve the Navier-Stokes equations alongside the potential and bioheat ones during each simulation in order to maintain a design flexible enough to handle also more complex (i.e. fully coupled) situations, such as a stress tensor of the tissue that varies with temperature.*

4.2   *In-vitro* experimental setup

Two *in-vitro* sets of experiments using porcine myocardial tissue were performed in an experimental setup similar to the one presented in [2]. The porcine myocardial tissue was placed on a polymethyl methacrylate board in a bloodbath. An iron arm attached to the board kept the catheter perpendicular to the tissue and maintained the contact force around the target $10\,\text{g}$, $20\,\text{g}$ and $40\,\text{g}$, as measured by the catheter system. A pump attached to the iron arm generated a constant blood flow of $0.5\,\text{m/s}$. The indifferent electrode was placed at the bottom of the blood bath. A heater preserved the blood temperature to $37\,^{\circ}\text{C}$.

The 6-holes open-irrigated TactiCath Quartz catheter by St. Jude Medical Inc. was used in the experiment. A constant power delivery ablation protocol of $20\,\text{W}$ or $35\,\text{W}$ was followed for all the ablations and a saline flow rate of $17\,\text{mL/min}$ was set.

After the radiofrequency delivery, the lesion dimensions were assessed by examining their cross-section. The measured variables were the depth (D), the width (W) and the depth of the maximum width (DW) as shown in Figure 4. In standard computational models that feature a sharp insertion of the catheter in the tissue, the depth and depth of maximum width are measured from the tissue surface. However, such measurement techniques have their limitations. First, existing computational models do not take into account the irregular surface of the cardiac wall, and neither do we at this stage. In addition, since lesions are assessed after physical manipulation, it is difficult to identify the actual position of the pre-ablation tissue surface. By considering these limitations, we opted to use measurements that allow us to validate our numerical results through comparable variables (see Figure 4 and Figure 5, right).

A total of 31 ablations were performed for different target experimental setups, using three control parameters: the contact force F, the applied power P and the time of ablation T. During
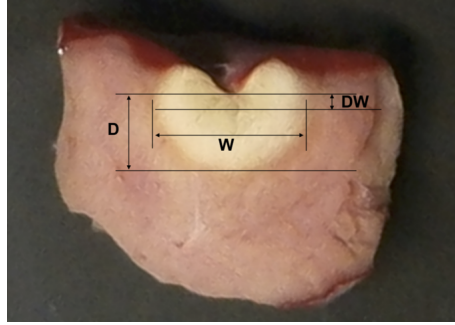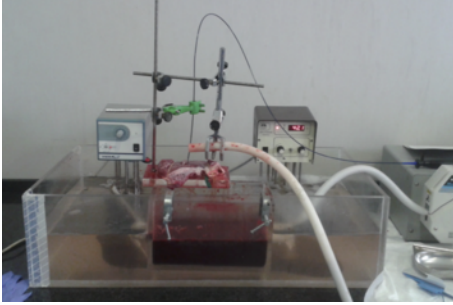
Figure 4: Left: the experimental setup. Right: lesion measurements: depth (D), width (W) and depth of maximum width (DW).

	Target experimental setup (F, P, T)			
	$(10^*\mathrm{g}, 20\mathrm{W}, 30\mathrm{s})$	$(10^*\mathrm{g}, 35\mathrm{W}, 30\mathrm{s})$	$(20^*\mathrm{g}, 20\mathrm{W}, 30\mathrm{s})$	$(40^*\mathrm{g}, 20\mathrm{W}, 30\mathrm{s})$
n	8	5	9	2
$\bar{F}_{exp}$ (g)	11.2 [11.1 : 11.5]	11.9 [11.3 : 12.0]	19.9 [19.6 : 22.2]	41.0 [40.5 : 41.5]
D (mm)	2.3 [1.8 : 2.6]	4.4 [4.3 : 4.6]	3.1 [2.8 : 3.5]	3.3 [3.0 : 3.5]
min	1.4	4.2	2.2	3.0
max	3.1	4.6	4.6	3.5
W (mm)	6.5 [6.3 : 7.4]	12.7 [9.9 : 13.2]	8.9 [8.0 : 10.5]	7.2 [7.1 : 7.2]
min	5.5	8.4	7.0	7.1
max	7.9	14.1	11.7	7.2
DW (mm)	0.4 [0.4 : 0.7]	0.4 [−0.1 : 0.9]	0.5 [0.3 : 0.8]	0.7 [0.3 : 1.0]
min	0.3	−1.0	−0.6	0.3
max	0.8	1.0	1.4	1.0
R_0 (Ω)	121 [116 : 134]	104 [102 : 138]	122 [114 : 124]	127 [117 : 136]

Table 2: Summary of lesion dimensions for every experimental setup. The starred values * denote the mean nominal forces and include a standard deviation of 1 g. The values in the table are either absolute numbers or expressed in the format Q_2 [Q_1 : Q_3], where Q_2 is the median and Q_1 and Q_3 are the first and the third quartiles.

the experiments we observed that the target contact force was not always achieved due to maneuvrability limitations and the effect of the blood inflow to the system. Thus, we allow a standard deviation of 1 g as error of the mean experimental force F_{exp} around the nominal force F and we remove the observations that deviate three standard deviations. Table 2 summarizes the lesion dimensions and the initial impedance of the system R_0. The mean experimental contact force $\bar{F}_{exp}$ is reported for the non-extreme cases. No complications (steam pops, char formation etc.) were observed in our experiments.

4.3 Model validation

We validate our model by comparing the computational lesion dimensions against the *in-vitro* experimental results in Section 4.2. We run simulations with parameters corresponding to the first 3 settings of the experiments. We discarded the (40g, 20W, 30s) configuration because only two experiments were available, and one of the two images obtained from the experiments was too blurry to get solid measurements. As an example, in Figure 5 we show the 3D lesion computed in the (20g, 20W, 30s) settings, and the corresponding lesion dimensions used for validation. Given the uncertainty on the cross-section orientation (with respect to the blood flow direction) of the experimental lesions, these dimensions are assessed on the plane featuring the maximum width of the lesion.
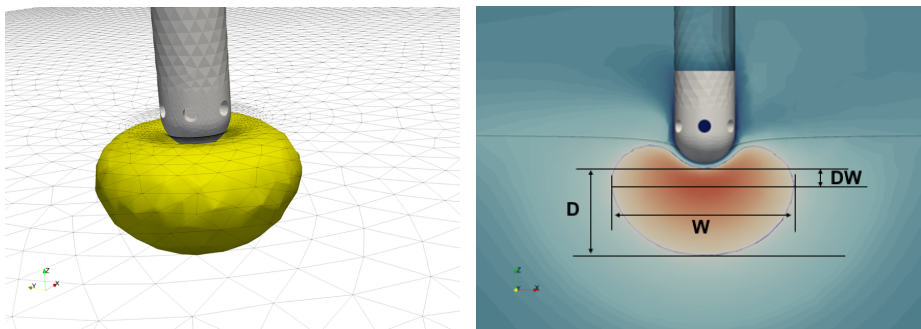

Figure 5: Left: the 3D computed lesion in the (20g, 20W, 30s) settings. Right: lesion measurements used for validation.

In Table 3 we collect the resulting lesion dimensions of our numerical simulations. We observe that the depth D, the width W and the depth of the maximum width DW of the computational lesion are within the range of the corresponding experimental values for the case of $F = 20\,\mathrm{g}$. In the 10 g cases, the lesion width is underestimated by around 10% for both cases. Furthermore, the depth of the maximum width is overestimated by nearly 50% for the case of $P = 35\,\mathrm{W}$.

	Computational setup $(F,\,P,\,T)$		
	$(10\mathrm{g}, 20\mathrm{W}, 30\mathrm{s})$	$(10\mathrm{g}, 35\mathrm{W}, 30\mathrm{s})$	$(20\mathrm{g}, 20\mathrm{W}, 30\mathrm{s})$
D (mm)	2.58	4.25	3.69
min − max	✓	✓	✓
W (mm)	4.88	7.63	7.25
min − max	−11.27%	−9.17%	✓
DW (mm)	0.80	1.47	1.01
min − max	✓	+47%	✓

Table 3: Comparison of the computational lesions against the range of the experimental data.

To dwell deeper into the width underestimation (a feature already observed in [17]), we compare the computational lesion dimensions against the interquartile range $Q_1 - Q_3$. The results are shown in Table 4. By comparing Table 3 and Table 4, it can be seen that the depth of maximum lesion

15

	Computational setup (F, P, T)		
	$(10\mathrm{g}, 20\mathrm{W}, 30\mathrm{s})$	$(10\mathrm{g}, 35\mathrm{W}, 30\mathrm{s})$	$(20\mathrm{g}, 20\mathrm{W}, 30\mathrm{s})$
D (mm)	2.58	4.25	3.69
$Q_1 - Q_3$	✓	-1.16%	$+5.42\%$
W (mm)	4.88	7.63	7.25
$Q_1 - Q_3$	-22.53%	-22.93%	-9.37%
DW (mm)	0.80	1.47	1.01
$Q_1 - Q_3$	$+14.28\%$	$+52.22\%$	$+26.25\%$

Table 4: Comparison of the computational lesions against the interquartile range $Q_1 - Q_3$ of the experimental data.

width is consistently overestimated with respect to the experimental interquartile range, while the lesion width is underestimated. The $(10\,\mathrm{g},\,35\,\mathrm{W},\,30\,\mathrm{s})$ setting shows a tiny deviation from the experimental lesion depth, however the experimental results show a very narrow interquartile range of $0.3\,\mathrm{mm}$. For the other settings, the depth of the lesion lies in the upper part the interquartile range or is overestimated by 5%. Nonetheless, the lesion width is always underestimated while the depth of the maximum width is overestimated up to $52.22\,\%$. This shows that the computational lesion is more spherical than the experimental one. One possible explanation for this is that our hypothesis of isotropic heat diffusion in the tissue is not good enough for the type of prediction we are trying to make. After all, it is a known fact that cardiac tissue is not isotropic itself, being made of layers of fibers that run parallel to the surface of the heart, and rotate clockwise by almost 120 degrees between the endocardium (where the electrode is in contact with the tissue), and the epicardium [43, 44]. It is thus worth investigating further the anisotropy of the tissue's thermal [45] and electrical conductivities [49]. This aspect is currently under study.

4.4   Comparison of elastic and sharp insertions

One of the strengths (and novelties) of the proposed methodology resides in resorting to an elastic model for the tissue, which allows us to treat in a systematic manner both the deformation of the tissue and the power dissipated in it. The more accurate description of the tissue-electrode contact surface provided by the elastic model reflects into a more precise evaluation of the power dissipated into the tissue with respect to models featuring a sharp insertion of the catheter into an undeformed tissue. The latter is the common configuration encountered in the available literature: besides being pretty unphysical in itself, it relies on somewhat arbitrary levels of insertion in the tissue, which are never clearly explained. In addition, a sharp insertion configuration features a larger contact surface between the tissue and the electrode. Since the power delivered to the tissue depends on the percentage of electrode surface in contact with the tissue, a sharp insertion is very likely to overestimate the tissue temperature rise and, in consequence, the lesion size. To highlight this aspect, we considered two different computational geometries: an elastic deformed tissue and a sharp insertion one. In the two geometries, the catheter is placed at the same depth with respect to the undeformed tissue state. Figure 6 shows the two different computational geometries for $10\,\mathrm{g}$, $20\,\mathrm{g}$ and $40\,\mathrm{g}$ pressure.

We simulate an ablation protocol of $20\,\mathrm{W}$ for $30\,\mathrm{s}$, where we use the tissue parameters of a porcine myocardium and we consider, inspired from existing experimental studies [20], two different
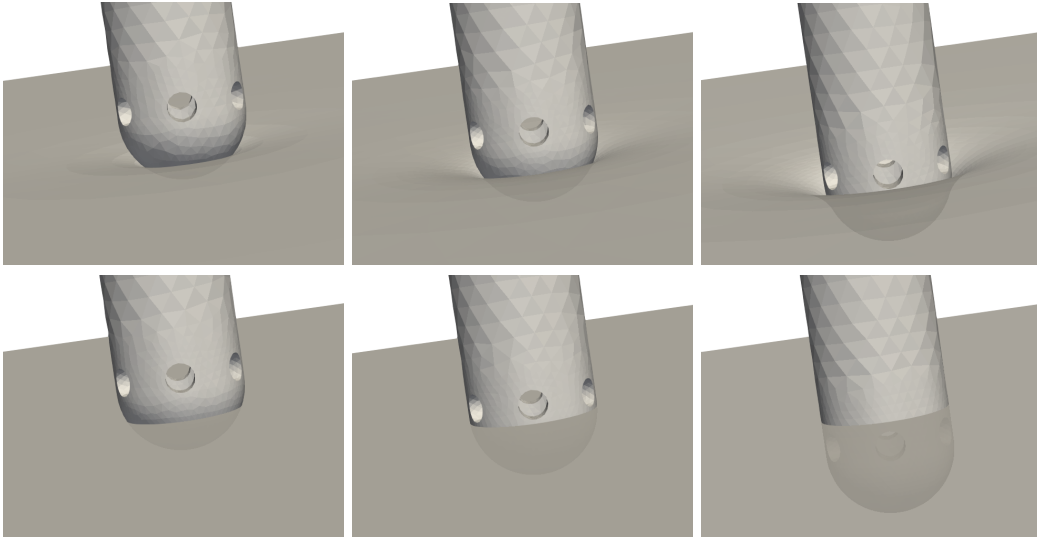
Figure 6: Elastic (top row) and sharp (bottom row) catheter insertion for 10g (left), 20g (middle), and 40g (right) pressure.

simulation protocols with respect to the imposed blood flow velocity: a High-Flow protocol (HF), with $u_b = 0.5 \, \mathrm{m/s}$, and a Low-Flow protocol (LF), with $u_b = 0.1 \, \mathrm{m/s}$. In Figure 7 we show the impact of the two protocols on the streamlines of the saline coolant stemming from the irrigation holes in the elastic $20 \, \mathrm{g}$ pressure case.
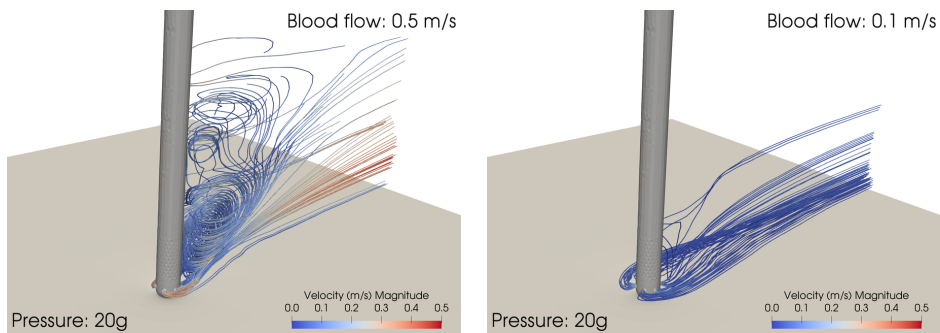

Figure 7: **High-Flow and Low-Flow protocols.** Streamlines of the saline flow from the irrigation holes for the High-Flow (left) and Low-Flow (right) protocols for a catheter pressure of $20 \, \mathrm{g}$.

In Tables 5 and 6 we report the percentage α of power delivered to the tissue as well as the resulting computational lesion characteristics for the two insertion profiles in the high blood flow and low blood flow protocols, respectively. The tissue power percentage is calculated as described in Section 3.1.1. Due to the difference in the contact surface area of the electrode with the tissue, the power delivered to the tissue in the sharp insertion case is more than twice the one of the

17

(20W, 30s)		10g		20g		40g	
		elastic	sharp*	elastic	sharp*	elastic	sharp*
α	(%)	8.46	18.87	13.29	30.73	19.91	54.57
D	(mm)	2.58	4.16	3.69	2.61	4.39	2.07
W_x	(mm)	4.79	7.67	7.00	6.61	9.11	6.62
W_y	(mm)	4.84	7.88	7.22	6.71	9.11	6.57
DW_x	(mm)	0.80	1.52	0.91	0.11	0.93	-1.12
DW_y	(mm)	0.80	1.32	1.01	0.21	0.93	-1.12
V	(mm^3)	38.28	162.6	123.55	88.33	260.15	92.44
S	(mm^2)	0	0	0	0	0	0.63
T_{max}	(°C)	61.22	>100	76.95	>100	93.17	>100
Pop time	(s)	-	21.6	-	5.4	-	2.5

Table 5: **High-Flow protocol**. Lesion characteristics for sharp and elastic insertion. * Simulation stopped as a pop: lesion characteristics were assessed at pop time.

(20W, 30s)		10g		20g		40g	
		elastic	sharp*	elastic	sharp*	elastic	sharp*
α	(%)	8.46	18.87	13.29	30.73	19.91	54.57
D	(mm)	2.46	4.17	3.62	2.63	4.38	2.09
W_x	(mm)	4.44	7.74	6.69	6.77	9.08	6.76
W_y	(mm)	4.41	7.91	6.86	6.83	9.21	6.70
DW_x	(mm)	0.68	0.78	0.84	0.04	0.91	-1.50
DW_y	(mm)	1.03	1.33	1.04	-0.26	0.91	-1.20
V	(mm^3)	31.28	166.33	107.14	94.20	263.54	101.94
S	(mm^2)	0	0	0	0.07	0	11.84
T_{max}	(°C)	60.43	>100	75.66	>100	92.64	>100
Pop time	(s)	-	21.7	-	5.3	-	2.4

Table 6: **Low-Flow protocol**. Lesion characteristics for sharp and elastic insertion. * Simulation stopped as a pop occurred: lesion characteristics were assessed at pop time.

elastic case. Moreover, as this ratio grows with the insertion depth (2.15, 2.33, and 2.41 times for the 10 g, 20 g and 40 g cases, respectively), the tissue temperature rise is expected to be more rapid and overestimated. The lesion depth is assessed as in the previous section. Concerning lesion width and depth of maximal width, we split the measurement in two: one along the direction of the blood flow (W_x at depth DW_x), the other orthogonal to it (W_y at depth DW_y). This choice allows us to assess the difference in lesion anisotropy between the two cases. Finally, the lesion volume and surface area are assessed computing the volume enclosed by the 50 °C isothermal surface in the tissue, and the area intercepted on the tissue surface by the same isothermal surface.

From Tables 5 and 6 we can observe that the sharp insertion geometry produces consistently larger maximum temperatures and steam pops, as expected from the bigger percentage of power delivered to the tissue. In the case of elastic 10 g, the maximum tissue temperature is approximately

60 °C for both protocols. On the contrary, a maximum temperature of 100 °C is reached for the sharp cases after 21.6 s, hinting for the occurrence of steam pops. For both blood flow protocols, the lesion size before popping is much larger than the one developed using an elastic deformation of the tissue. In the 20 g and 40 g cases, the sharp insertion cases have a very rapid temperature increase to 100 °C in only 5.4 s and 2.5 s respectively, hinting for the occurrence of steam pops. However, a lesion is formed using the elastic tissue and the temperature is below 100 °C after the completion of 30 s. This comes in good agreement with our *in-vitro* experimental results, where no steam pops were observed in the 20 g and 40 g cases (see Section 4.2). In Figures 8 and 9 we compare, for both High and Low-Flow protocols, the lesions obtained at the end of the simulation (or at the time of popping). The clipping plane for both figures is the diagonal of the computational domain. The temperature scale is the same for all plots to help visualization. The black spots in the sharp insertion cases highlight the pop location.

Finally, we explore the impact of the high and low blood flow protocols on the elastic cases. It appears that smaller lesions are created in the Low-Flow protocol for 10 g force, while for stronger catheter contact forces such as 40 g the lesion size is similar for both protocols. This effect is a consequence of a larger portion of the catheter being in direct contact with the tissue and the fact that the lesion is formed deeper, thus temperature changes in blood-tissue interface have a negligible effect in the lesion size. For further investigation, we consider the lesion width along the x (along the blood flow) and y (perpendicular to the blood flow) directions to evaluate the lesion morphological changes. The High-Flow protocol produces lesions which are more symmetric, with the depth of the maximum width in the medial and lateral direction with respect to the flow being the same. However, differences in the symmetry of the lesion occur for the Low-Flow case. Figure 10 shows the temperature distribution for high and low blood flows for the elastic deformed tissue case and 10 g contact force. Note that the saline cooling effect dominates in the Low-Flow protocol, and leads to a different lesion morphology near the blood-tissue interface. In particular, a small change appears in the width of the lesion in the medial direction with respect to the flow, without affecting the symmetry of the lesion shape. A more evident change in the shape of the lesion appears in the lateral section, where the lesion appears to be tilted opposite to the blood flow due to the strong cooling effect of the irrigated saline. This effect becomes less evident for higher contact force profiles, such as 20 g and 40 g, and the lesion symmetry is restored in both the medial and lateral directions.

5   Discussion and future work

In this paper we propose a novel framework to model the radiofrequency catheter ablation process, which aims at surpassing important limitations of state of the art models. First, our approach does not only consider the biophysical, but also the mechanical properties of the cardiac tissue. The model captures the elastic deformation that is produced on the tissue when the catheter exerts a pressure on the cardiac wall. An accurate modelling of the catheter geometry allows to account for a more realistic interaction between the coolant liquid springing from the open-irrigated catheter and the blood flow. The addition of a board between the cardiac tissue and the dispersive electrode has a double motivation. On the one hand, neither in *in-vitro* experiments nor in clinical settings the dispersive electrode is placed in direct contact with the ablated tissue: assuming a direct contact would therefore lead to an excessive simplification of the model. On the other hand, the presence of the board allows us to use as much information as possible from the
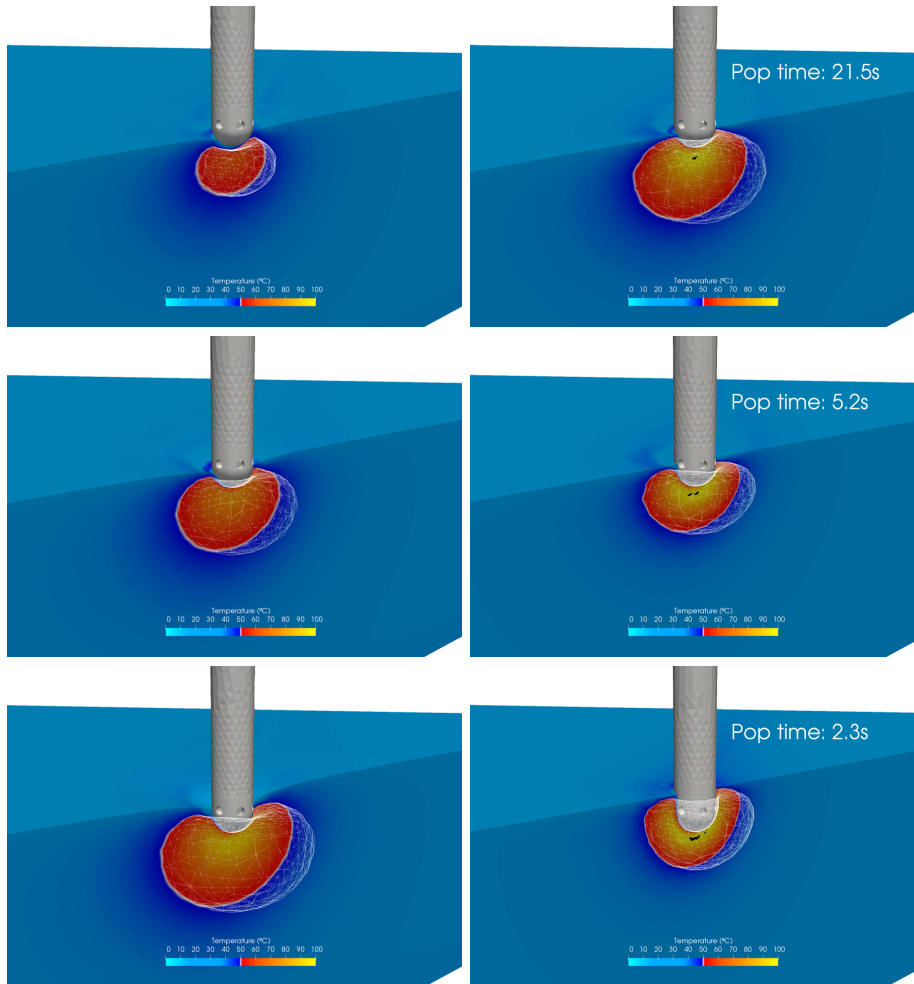
19

Figure 8: **High-Flow protocol.** Tissue heating with elastic (left column) and sharp (right column) catheter insertions for different values of pressure. The 3D lesions are highlighted by the white wireframes. The black spots in the right panels highlight the steam pop location. Top row: 10 g. Middle row: 20 g. Bottom row: 40 g. The temperature scale is the same for all plots. Simulation protocol: 20 W, 30 s.
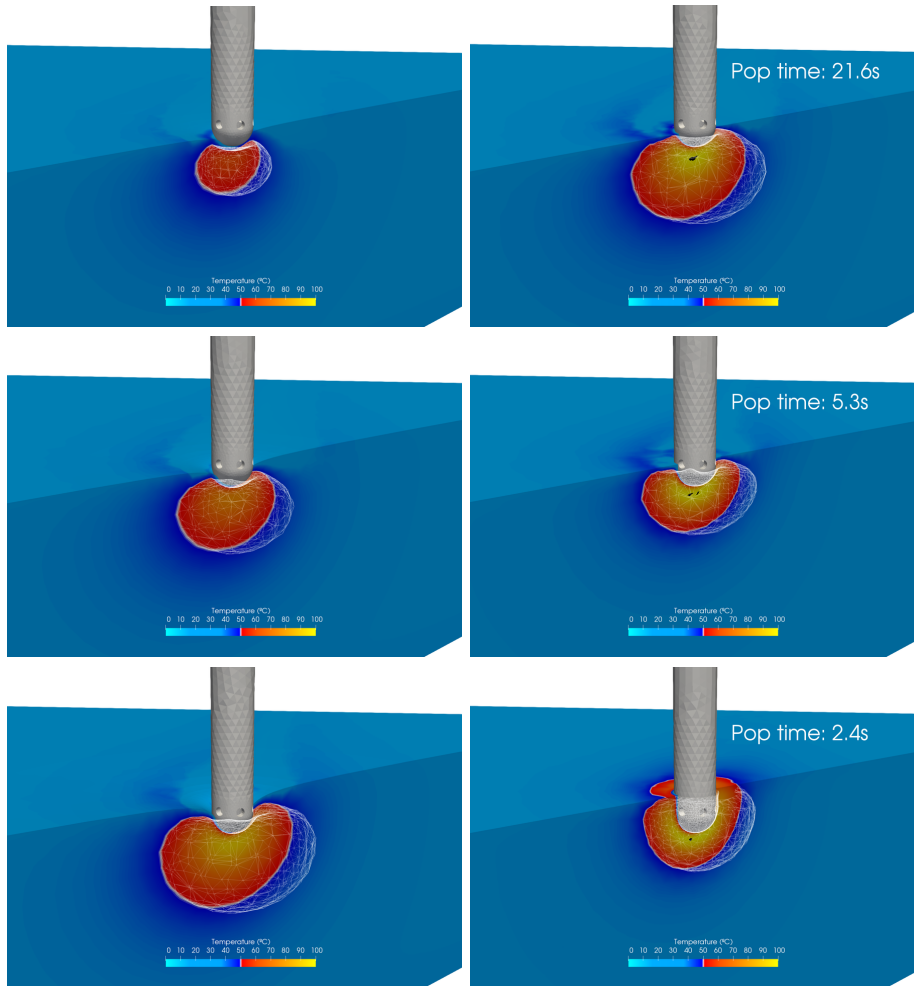
Figure 9: **Low-Flow protocol.** Tissue heating with elastic (left column) and sharp (right column) catheter insertions for different values of pressure. The 3D lesions are highlighted by the white wireframes. The black spots in the right panels highlight the steam pop location. Top row: 10 g. Middle row: 20 g. Bottom row: 40 g. The temperature scale is the same for all plots. Simulation protocol: 20 W, 30 s.
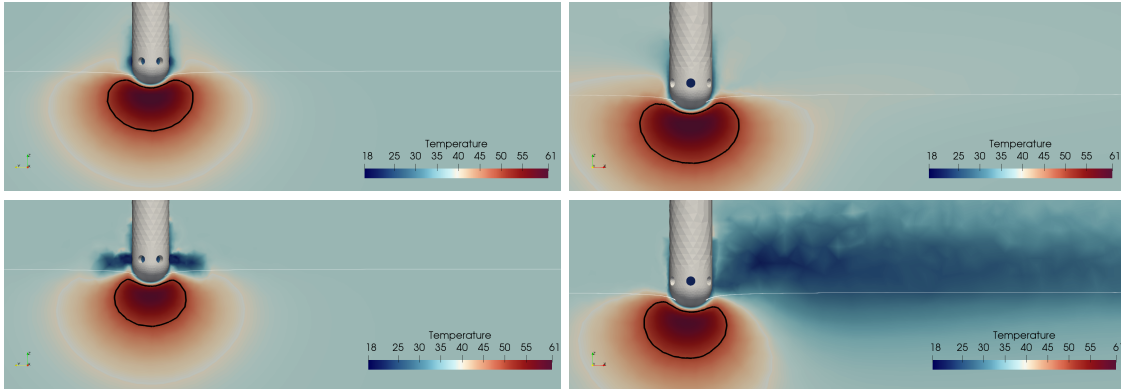
Figure 10: **High-Flow vs Low-Flow.** The effect of the High-Flow (Top) and Low-Flow (Bottom) protocol in the medial (Left) and lateral (Right) for the elastic catheter insertion case. The computational lesion is displayed in black outline. Simulation protocol: $10\,\text{g}$, $20\,\text{W}$, $30\,\text{s}$.

RFA system: by properly tuning the board conductivity, we can match both the appropriate power delivered to the tissue and the overall system impedance, without the need to modify the tissue conductivity. Finally, the amount of power dissipated in the tissue is computed as a function of the surface of contact between the electrode and the tissue itself. The computational model relies on open-source software, from geometry construction to numerical simulations, and postprocessing. In particular, Salome (*http://www.salome-platform.org*) was used for mesh generation, FEniCS-HPC (*http://www.fenics-hpc.org*) for the numerical solution of the PDE system and Paraview (*http://www.paraview.org*) for the postprocessing of the numerical results and the visualizations.

The computational model has been validated in comparison with two sets of *in-vitro* experiments, featuring 3 different ablation protocols: $(10\,\text{g}, 20\,\text{W}, 30\,\text{s})$, $(10\,\text{g}, 35\,\text{W}, 30\,\text{s})$, $(20\,\text{g}, 20\,\text{W}$ and $30\,\text{s})$. The numerical lesions have been assessed against the experimental ones through some characteristic dimensions such as lesion depth, width and depth of maximum width. The simulated lesions are globally in good agreement with the experimental measurements. In particular, the lesion depth always lies within the range of the corresponding experimental results, but the lesion width can be underestimated. A significant difference is observed in the $10\,\text{g}$ ablation simulation, where the lesion width is underestimated by around $10\,\%$, and in the depth of the maximum width for the $35\,\text{W}$ case, which is overestimated by nearly 50%. A more careful comparison with the interquartile $Q_1 - Q_3$ of the experimental results (see Table 4) shows that the depth of maximum lesion width is overestimated while the lesion width is underestimated. The simulated lesion is thus consistently more spherical than the experimental one, prompting for further investigation to clarify this issue. This shortcoming can be a consequence of the isotropic heat diffusion coefficient we used in this paper: given the lack of isotropy in the cardiac tissue itself, we are currently investigating possible anisotropies in the model parameters, in particular the thermal [45] and electrical conductivities [49].

We then compared the effect of using an elastic deformation of the tissue under the catheter pressure against profiles featuring a sharp insertion. Accounting for tissue elasticity provides a realistic relation between the contact force and the indentation depth in the cardiac tissue. As a consequence, the actual power dissipated in the tissue can be computed in a systematic manner,

22

differently from other state-of-the-art models featuring sharp-insertion configurations, where it is unclear how the same information is deduced. We compared the two insertion profiles by placing the catheter at the same depth with respect to the undeformed tissue. The larger amount of tissue surface in contact with the electrode in the sharp insertion case leads to a systematic overestimation of the temperature rise in the tissue. To highlight this aspect we simulated an ablation of 20 W for 30 s on a porcine myocardium, with contact forces of 10 g, 20 g and 40 g, and two different blood flow protocols. The sharp insertion cases consistently reach 100 °C in less than 30 s, which are unphysical taken into account our *in-vitro* experimental results, where no steam pops occurred. Furthermore, in the 40 g case, the saline irrigation holes are submerged in the cardiac tissue for a sharp profile, contrary to what has been observed during our *in-vitro* experiments. A visual inspection on the simulated lesions shows that the elastic deformation case produces lesions that are closer in shape to the ones obtained in the experiments.

Finally, we compared the effect of the high and low blood flow protocols on the resulting lesions in the elastic case. It appears that the Low-Flow protocol produces smaller lesions for contact forces of 10 g and 20 g, while the lesion size in both protocols are comparable for a contact force of 40 g in both protocols. In addition, we explored the morphological changes of the lesion between the two types of blood flows. For a contact force of 10 g, the Low-Flow protocol affects the lesion orientation, which becomes tilted opposite to the blood flow in the lateral direction due to the cooling of the irrigated saline. This effect becomes less evident as the contact force increases, and for 40 g contact force the lesion symmetric shape is practically restored.

As accurate predictions of the lesions generated by radiofrequency cardiac ablation are fundamental to devise possible new interventional strategies, the use of elastic deformation for the tissue presented in this paper is a significant step towards a more realistic description. However, a number of limitations are still present. First, we considered an isotropic and homogeneous cardiac tissue, even though the myocardium structure is highly complex and its surface is not smooth [46]. In addition, the deformations are assumed to lie within the elastic bound of the tissue, however it is evident in the experimental lesions that an elasto-plastic contact occurs. This might be a result of the temperature change, which alters the mechanical properties of the tissue, an aspect worth investigating. Finally, in this work we considered is constant Young's modulus of elasticity, even though a dependency on the heart cycle (systole or diastole) has been observed [31]. The effect of the Young's modulus of elasticity in the proposed RFA model is currently under investigation.

References

[1] Huang Shoei K Stephen, Wood Mark A. *Catheter Ablation of Cardiac Arrhythmias E-book.* Elsevier Health Sciences; 2014.

[2] Guerra Jose M., Jorge Esther, Raga Silvia, et al. Effects of open-irrigated radiofrequency ablation catheter design on lesion formation and complications: in vitro comparison of 6 different devices. *Journal of Cardiovascular Electrophysiology.* 2013;24(10):1157–1162.

[3] Demolin Julie M., Eick Olaf J., Munch Kuno, Koullick Edouard, Nakagawa Hiroshi, Wittkampf Fred H.M.. Soft Thrombus Formation in Radiofrequency Catheter Ablation. *Pacing and Clinical Electrophysiology.* 2002;25(8):1219–1222.

[4] Haines D.E., Verow A.F. Observation on electrode-tissue interface temperature and effect on electrical impedance during radiofrequency ablation of ventricular myocardium. *Circulation.* 1990;82 (3):1034–1038.

[5] Koruth Jacob S., Dukkipati Srinivas, Gangireddy Sandeep, et al. Occurrence of steam pops during irrigated RF ablation: Novel insights from Microwave Radiometry. *Journal of Cardiovascular Electrophysiology.* 2013;24(11):1271–1277.

[6] Chik William W.B., Kosobrodov Roman, Bhaskaran Abhishek, et al. Acoustic Signal Emission Monitoring as a Novel Method to Predict Steam Pops During Radiofrequency Ablation: Preliminary Observations. *Journal of Cardiovascular Electrophysiology.* 2015;26(4):440–447.

[7] Labonte Sylvain. Numerical model for radio-frequency ablation of the endocardium and its experimental validation. *IEEE Transactions on Biomedical Engineering.* 1994;41(2):108–115.

[8] Shimko N, Savard P, Shah K. Radio frequency perforation of cardiac tissue: modelling and experimental results. *Medical and Biological Engineering and Computing.* 2000;38(5):575–582.

[9] Tungjitkusolmun S, Woo EJ, Cao H, Tsai JZ, Vorperian VR, Webster JG. Thermal-electrical finite element modelling for radio frequency cardiac ablation: effects of changes in myocardial properties. *Medical and Biological Engineering and Computing.* 2000;38(5):562–568.

[10] Berjano Enrique J, Hornero Fernando. Thermal-electrical modeling for epicardial atrial radiofrequency ablation. *IEEE transactions on biomedical engineering.* 2004;51(8):1348–1357.

[11] Irastorza Ramiro M, d'Avila Andre, Berjano Enrique. Thermal latency adds to lesion depth after application of high-power short-duration radiofrequency energy: Results of a computer-modeling study. *Journal of cardiovascular electrophysiology.* 2018;29(2):322–327.

[12] González-Suárez Ana, Pérez Juan J, Berjano Enrique. Should fluid dynamics be included in computer models of RF cardiac ablation by irrigated-tip electrodes?. *Biomedical engineering online.* 2018;17(1):43.

[13] Panescu Dorin, Whayne James G, Fleischman Sidney D, Mirotznik Mark S, Swanson David K, Webster John G. Three-dimensional finite element analysis of current density and temperature distributions during radio-frequency ablation. *IEEE Transactions on Biomedical Engineering.* 1995;42(9):879–890.

[14] Berjano Enrique J. Theoretical modeling for radiofrequency ablation: state-of-the-art and challenges for the future. *Biomedical engineering online.* 2006;5(1):24.

[15] Gallagher Neal P., Fear Elise C., Vigmond Edward J., Byrd Israel A.. Cathether contact geometry affects lesion formation in radio-frequency cardiac catheter ablation. *Proceedings of the Annual International Conference of the IEEE Engineering in Medicine and Biology Society, EMBS.* 2011;8(9):243–246.

[16] Gopalakrishnan Jayadeep. A mathematical model for irrigated epicardial radiofrequency ablation. *Annals of biomedical engineering.* 2002;30(7):884–893.

[17] González-Suárez A., Berjano E., Guerra J. M., Gerardo-Giorda L.. Computational modeling of open-irrigated electrodes for radiofrequency cardiac ablation including blood motion-saline flow interaction. *PloS one.* 2016;11(3):e0150356.

[18] Wittkampf Fred HM, Nakagawa Hiroshi. RF catheter ablation: Lessons on lesions. *Pacing and Clinical Electrophysiology.* 2006;29(11):1285–1297.

[19] Cao Hong, Speidel Michael A, Tsai Jang-Zern, Van Lysel Michael S, Vorperian Vicken R, Webster John G. FEM analysis of predicting electrode-myocardium contact from RF cardiac catheter ablation system impedance. *IEEE Transactions on Biomedical Engineering.* 2002;49(6):520–526.

[20] Guerra Jose M, Jorge Esther, Raga Silvia, et al. Effects of Open-Irrigated Radiofrequency Ablation Catheter Design on Lesion Formation and Complications: In Vitro Comparison of 6 Different Devices. *Journal of Cardiovascular Electrophysiology.* 2013;24(10):1157–1162.

[21] Jiang Yansheng, Possebon Ricardo, Mulier Stefaan, et al. A methodology for constraining power in finite element modeling of radiofrequency ablation. *International Journal for Numerical Methods in Biomedical Engineering.* 2017;33(7).

[22] Pérez Juan J, González-Suárez Ana, Berjano Enrique. Numerical analysis of thermal impact of intramyocardial capillary blood flow during radiofrequency cardiac ablation. *International Journal of Hyperthermia.* 2017;(just-accepted):1–25.

[23] Asaro Robert, Lubarda Vlado. *Mechanics of solids and materials.* Cambridge University Press; 2006.

[24] Popov Valentin L.. *Contact mechanics and friction.* Springer; 2010.

[25] Yoffe EH. Modified Hertz theory for spherical indentation. *Philosophical Magazine A.* 1984;50(6):813–828.

[26] Sneddon Ian N. The relation between load and penetration in the axisymmetric Boussinesq problem for a punch of arbitrary profile. *International journal of engineering science.* 1965;3(1):47–57.

[27] Hasgall P.A., Neufeld E., Gosselin M.C., Klingenböck A., Kuster N.. ITIS Database for Thermal and Electromagnetic Parameters of Biological Tissues. *Version 3.0.* 2015;.

[28] Tsai Jang-Zern, Will James A, Hubbard-Van Stelle Scott, et al. In-vivo measurement of swine myocardial resistivity. *IEEE Transactions on Biomedical Engineering.* 2002;49(5):472–483.

[29] Duck Francis A. *Physical properties of tissues: a comprehensive reference book*. Academic press; 2013.

[30] Bhavaraju NC, Valvano JW. Thermophysical properties of swine myocardium. *International journal of thermophysics*. 1999;20(2):665–676.

[31] Couade Mathieu, Pernot Mathieu, Tanter Mickael, et al. Quantitative imaging of myocardium elasticity using supersonic shear imaging. In: :151–154IEEE; 2009.

[32] Wells Peter NT, Liang Hai-Dong. Medical ultrasound: imaging of soft tissue strain and elasticity. *Journal of the Royal Society Interface*. 2011;8(64):1521–1549.

[33] Nédélec Jean-Claude. *Acoustic and electromagnetic equations: integral representations for harmonic problems*. Springer Science & Business Media; 2001.

[34] Jones Eric, Oliphant Travis, Peterson Pearu. SciPy: Open source scientific tools for Python. *URL http://www. scipy. org*. 2001–;.

[35] Ribes Andre, Caremoli Christian. Salome platform component model for numerical simulation. In: :553–564IEEE; 2007.

[36] Hoffman Johan, Jansson Johan, Jansson Niclas, De Abreu Rodrigo Vilela, Johnson Claes. Computability and adaptivity in CFD. *Encyclopedia of Computational Mechanics Second Edition*. 2017;:1–22.

[37] Logg Anders, Mardal Kent-Andre, Wells Garth, al. . Automated solution of differential equations by the finite element method. *Lecture Notes in Computational Science and Engineering*. 2012;84:1–736.

[38] Hoffman Johan, Jansson Johan, Jansson Niclas. FEniCS-HPC: Automated predictive high-performance finite element computing with applications in aerodynamics. *Proceedings of the 11th International Conference on Parallel Processing and Applied Mathematics, PPAM 2015. Lecture Notes in Computer Science*. 2015;.

[39] Hoffman Johan, Jansson Johan, Abreu Rodrigo Vilela, et al. Unicorn: Parallel adaptive finite element simulation of turbulent flow and fluid–structure interaction for deforming domains and complex geometry. *Computers & Fluids*. 2013;80:310–319.

[40] Jansson Johan, Krishnasamy Ezhilmathi, Leoni Massimiliano, Jansson Niclas, Hoffman Johan. Time-Resolved Adaptive Direct FEM Simulation of High-Lift Aircraft Configurations. In: Springer 2018 (pp. 67–92).

[41] Quarteroni Alfio M, Valli Alberto. *Numerical Approximation of Partial Differential Equations*. Springer Publishing Company, Incorporated; 1994.

[42] Ayachit Utkarsh. *The paraview guide: a parallel visualization application*. Kitware, Inc.; 2015.

[43] Streeter D.. Gross morphology and fiber geometry in the heartch. 4, :61–112. In: Handbook of Physiology, Section 2: The cardiovascular systemAmerican Physiology Soc. 1979.

[44] Le Grice J., Smaill B.H., Chai L.Z., Edgar S.G., Gavin J.B., Hunter P.J.. Laminar structure of the heart: ventricular myocyte arrangement and connective tissue architecture in the dog. *Am. J. Physiol.*. 1995;269 (2 Pt. 2):H571–H582.

[45] Bhattacharya A, Mahajan RL. Temperature dependence of thermal conductivity of biological tissues. *Physiological measurement.* 2003;24(3):769.

[46] Ho Siew Yen, Sanchez-Quintana Damian, Cabrera Jose Angel, Anderson Robert H. Anatomy of the left atrium: implications for radiofrequency ablation of atrial fibrillation.. *Journal of cardiovascular electrophysiology.* 1999;10(11):1525–1533.

[47] Urban Matthew W, Pislaru Cristina, Nenadic Ivan Z, Kinnick Randall R, Greenleaf James F. Measurement of viscoelastic properties of in vivo swine myocardium using lamb wave dispersion ultrasound vibrometry (LDUV). *IEEE transactions on medical imaging.* 2013;32(2):247–261.

[48] Ramadan Sherif, Paul Narinder, Naguib Hani E. Standardized static and dynamic evaluation of myocardial tissue properties. *Biomedical Materials.* 2017;12(2):025013.

[49] Xie Fei, Zemlin Christian W. Effect of twisted fiber anisotropy in cardiac tissue on ablation with pulsed electric fields. *PloS one.* 2016;11(4):e0152262.